A Hybrid Sensor Based Backstepping Control Approach with its Application to Fault-Tolerant Flight Control

L. G. Sun[1] and C. C. de Visser[2], Q. P. Chu[3], and W. Falkena[4]
Delft University of Technology, Delft, 2600 GB, The Netherlands

Recently, an incremental type sensor based backstepping (SBB) control approach, based on singular perturbation theory and Tikhonov's theorem, has been proposed. This Lyapunov function based method uses measurements of control variables and less model knowledge, and it is not susceptible to the model uncertainty caused by fault scenarios. In this paper, the SBB method has been implemented on a fixed wing aircraft with its focus on handling structural changes caused by damages. A new hybrid autopilot flight controller has been developed for a Boeing 747-200 aircraft after combining nonlinear dynamic inversion (NDI) with SBB control approach. Two benchmarks for fault tolerant flight control (FTFC), named rudder runaway and engine separation, are employed to evaluate the proposed method. The simulation results show that the proposed control approach leads to a zero tracking-error performance in nominal condition and guarantees the stability of the closed-loop system under failures as long as the reference commands are located in the safe flight envelope.

---

[1] Ph.D. Student, Control and Simulation Devision, Faculty of Aerospace Engineering, P.O.Box 5058; l.sun@tudelft.nl, Student Member AIAA.

[2] Assistant Professor, Control and Simulation Devision, Faculty of Aerospace Engineering, P.O.Box 5058; C.C.deVisser@tudelft.nl, Member AIAA.

[3] Associate Professor, Control and Simulation Devision, Faculty of Aerospace Engineering, P.O.Box 5058; q.p.chu@tudelft.nl, Member AIAA.

[4] Ph.D. Student, Control and Simulation Devision, Faculty of Aerospace Engineering, P.O.Box 5058; W.Falkena@tudelft.nl, Student Member AIAA.

Nomenclature

b = wing span

$\bar{c}$ = mean aerodynamic chord, m

EPR = engine pressure ratio

he, xe, ye = position coordinates in earth fixed reference frame, m

I = moment of inertia matrix

P_c, P_d = collective and differential engine pressure ratio

$\mathbf{P_t}$ = a vector of total engine pressure ratios

p, q, r = roll, pitch and yaw rate around the body axis, rad/s

T = engine thrust, kN

V_{TAS} = true airspeed, m/s

α, β = angle of attack, angle of sideslip, deg

λ = integral term

ϕ, θ = roll angle, pitch angle, deg

δ_a, δ_e = deflection of aileron and elevator, deg

$\delta_{\text{ru}}, \delta_{\text{rl}}, \delta_{\text{sp}}$ = deflection of upper rudder, lower rudder and spoiler, deg

χ = heading angle, deg

γ = flight path angle, deg

ζ = damping ratio

ω_n = natural frequency, rad/s

ϵ = time scale tuning parameter, small positive constant

Subscripts

cmd = commanded values

CA = variable related to control allocation

des = control variables desired by the control algorithm

ir, il, or, ol = acronym of inboard right (wing), inboard left (wing), outboard right, outboard left

r = a reference command

I. Introduction

Research on previous flight accidents [1] and their corresponding fault tolerant flight control (FTFC) strategies suggests that an aircraft, under many post-failure circumstances, can still achieve a certain level of flight performance with the remaining valid control effectors. However, as a consequence of the structural/actuator failures, the control authority or the safe flight envelope of the aircraft is inevitably limited.

Among all fault scenarios, the incidents categorized as 'loss of control in flight' count for as much as 17% of all aircraft accidents [2], and have received most attention. These kinds of failures can be avoided by taking suitable control strategies [1] as suggested by the results of the Flight Mechanics Action Group 16 (FM-AG16), which is a branch of the Group for Aeronautical Research and Technology in Europe (GARTEUR). For example, an FTFC strategy, which involves a fault detection and isolation (FDI) block and a reconfigurable control block, makes it possible to remove the post-failure aircraft from danger [1, 3].

Much research has been done on FTFC in the past few decades. For the purpose of providing a validation platform for modern FDI and FTFC strategies, 6 fault scenarios have been embedded in the Reconfigurable Control for Vehicle Emergency Relief (RECOVER) benchmark model by the FM-AG 16 group including El Al flight 1862 (i.e.engine separation) and rudder runaway[1].

As suggested by Smaili et al. [1], Alwi and Edwards et al. [4] and Lombaerts and Smaili et al. [5], a powerful and advanced control approach is essential to increase the operational performance of the post-failure aircraft. The chosen control algorithms should have at least two of the following merits: it needs to be robust to the sudden structural changes of the aircraft, not relying on an accurate and full aerodynamic model, or it needs to contain a powerful model identification strategy by itself to provide all of the accurate model information for the FDI and reconfigurable control units in real-time.

A number of FDI methods, as well as reconfiguring control approaches, have been proposed in the literature [4, 6–10]. More recently, the work of Lombaerts et al. [5], as a part of the GARTEUR FM-AG 16 program, has provided practical validation results of a piloted adaptive nonlinear dynamic inversion (ANDI) controller on the Simulation, Motion, and Navigation (SIMONA) research simulator (SRS). The kernel of this work is a two-step online identification approach aiming at getting the physical model. In this work, rudder runaway case, El Al flight 1862 fault and stabilizer runaway scenarios were studied. The ANDI rate controller guarantees the stability of the post-failure aircraft and enables the pilot to land the aircraft safely. Thereafter, Alwi and Edwards et al.[4] validated another type of reconfigurable control method on the SRS, which was designed using a model reference sliding mode control method together with a constant control allocation matrix. In this work, only El Al flight 1862 scenario was evaluated. The sliding mode control method, which relies on relatively little information of the failure and the extent of the damage to the airframe, has also proven to be able to guarantee the stability of the closed-loop system subject to a certain class of model uncertainties (i.e.structural and actuator changes) caused by the separation of the right wing engines.

Except for utilizing the potential of the remaining control surfaces, researchers have also studied the feasibility of using the differential thrust in emergencies. In the case of rudder or vertical tail failure, the differential thrust control is an effective way to counteract the yawing moments induced by the stuck rudders and thus allow the aircraft to track heading angle commands [11]. A propulsion-controlled aircraft (PCA) system has been developed by the NASA Dryden Research Center, and was first evaluated on a piloted B-720 simulation [12]. In this PCA system, differential thrust was used as an emergency substitute for failed control surfaces [13] such as vertical tail loss with no rudder authority or rudder runaway case [11, 14]. Further research on the PCA system has been carried out by NASA Dryden and Ames Research Centers[14]. Many simulations and actual flight tests of different flight platforms have been performed.

In this paper, a sensor based backstepping (SBB) approach, which is capable of coping with aerodynamic model changes induced by the failure scenarios, is extended in its application and validated. In 2007, Hovakimyan et al.[15] proposed an advanced controller for non-affine systems, which involves the singular perturbation theory, Tikhonov's Theorem and a backstepping strategy. Thereafter, Falkena and van Oort et al. [16] extended its application and named it as SBB control approach. The SBB method was utilized to design a controller for the aircraft moment equations, and was also evaluated on an aerodynamic system with uncertainties and measurement noises. Indicated by [15, 16], as a result of the backstepping control technique, the system stability can be guaranteed by using Lyapunov functions in this SBB approach. In addition, similar to the incremental NDI flight control scheme, the SBB control approach does not need to adapt to uncertain parameters or unknown model structure, which is essential to most model-based conventional backstepping or NDI control approaches. The adaptation requirement is circumvented by using measurements of state derivatives rather than the full knowledge of the model, which is subject to structural or actuator changes.

The objective of this paper is to present an alternative reconfigurable control approach to the FTFC. This paper uses the SBB control approach proposed in [16], but the focus is shifted to extending its application to designing a generic attitude controller for a large civil aircraft and handling structural faults for FTFC purposes. In this paper, the SBB control law is utilized to design a body angular rate controller, while NDI control laws are adopted to design an outer loop angular controller. El Al flight 1862 scenario and rudder runaway fault case, which are challenging benchmark failure scenarios embedded in the RECOVER benchmark model, are utilized to validate the adaptation ability of the inner rate control loop. In rudder runaway case, the differential thrust of engines is introduced to generate necessary yawing moments in order to counteract the aerodynamic yawing moment produced by the stuck rudders. To make the flight simulation results more convincing, a regular flight path controller is also designed using PID control laws.

In Sec. II, the validation platform is introduced. Subsequently, the basic body angular rate motion equations and the NDI control method are provided in Sec. III. Thereafter, the single-loop body angular rate controller based on the sensor based backstepping (SBB) approach, as well as a hybrid NDI/SBB attitude hold/change controller, is presented in Sec. IV. In Sec. V, the simulation experiment results and the corresponding analysis are provided. Finally, concluding remarks are given by Sec. VI.

II. Validation Platform

The RECOVER benchmark model of Boeing 747-200 aircraft has been discussed in detail in [17, 18]. This high-fidelity benchmark model was developed for validating the advanced FTFC techniques, and it contains six benchmark fault scenarios:

1. stuck elevators (with/without turbulence)
2. stuck aileron (with/without turbulence)
3. stabilizer runaway (with/without turbulence)

4. rudder runaway (with/without turbulence)

5. loss of vertical tail

6. El Al failure case (dynamic/static method)

Among all of the failure scenarios, El Al flight 1862 scenario and rudder runaway fault case are the top two challenging cases[5], because they greatly cut down the safe flight envelope of the aircraft. Therefore, only these two fault scenarios will be applied to validate the new sensor based control method proposed in this paper.

A. Rudder Runaway and Engine Separation Scenarios

The losses and the remaining functional control surfaces in El Al flight 1862 are summarized as follows.

1. Lost surfaces due to the loss of hydraulic systems: outboard trailing-edge flaps, δ_{aor}, δ_{sp1} $\delta_{\text{sp4-5}}$, $\delta_{\text{sp8-9}}$, δ_{sp12},δ_{eil}, δ_{eor}.

2. Functional but affected surfaces: horizontal stabilizer (half trim rate), $\delta_{\text{air}}, \delta_{\text{ail}}$ (both at half rate), and the lower rudder δ_{rl} (lag).

3. Fully functional surfaces: inboard trailing-edge flaps, $\delta_{\text{sp2-3}}$, the left outboard elevator δ_{eol}, and the right inboard elevator δ_{eir}.

In the rudder runaway case, the rudder deflects to the left limit position, inducing a yawing tendency of the aircraft to the left. Since the aerodynamic blow-down is taken into account in the RECOVER simulation model, the rudder deflection limit of this scenario varies with the airspeed. As a result, the maximum rudder deflection is slightly below 15 *deg* for an airspeed of around 270 *kt* and close to 25 *deg* for an airspeed approaching 165 *kt*.

B. Overall Autopilot Flight Control System

An autopilot has been designed for the Boeing 747-200 aircraft, which has four control loops as shown in Fig. 1(a). In the fourth layer of this overall control diagram, an altitude controller is designed using the regular PID control law. In the third loop, a flight path controller has been designed using the regular PID control scheme, where $[\chi, \gamma, V]^\top$ are the controlled variables. $[\phi, \theta, \beta]^\top$ are controlled variables of the angular control loop in the second layer and $[p, q, r]^\top$ are the controlled variables of the first rate control loop. The airspeed is controlled by the collective engine pressure ratio (EPR) P_c. And P_d is the differential EPR used to actively generate a yawing moment. The spoilers are employed to assist the ailerons in order to enhance the control authority of the aircraft in the roll channel.

Assuming that the airspeed is able to be governed independently by regulating the engine thrust, the remaining most crucial thing in designing an autopilot flight path controller becomes designing a powerful and reliable angular controller (including rate controller). For the nominal case (i.e. fault-free) and the engine separation failure, a hybrid NDI/SBB angular controller has been designed using regular functional control surfaces without introducing the differential thrust. Compared with the incremental NDI, the advantage of the SBB rate controller is that it does not require the control effectiveness matrix, whose identification values are not adequately trustable during the transient period when sudden structural changes occur to the aircraft. The control structure is given in Fig. 1(b) with $\mathbf{u} = [\delta_a, \delta_e, \delta_r]^\top$ the control input vector. To handle the rudder runaway fault, the differential thrust has been introduced to counteract the yawing moment induced by the rudder, and a hybrid NDI/SBB attitude controller has been designed. The structure of this controller is depicted in Fig. 1(c), where $\mathbf{u} = [\delta_a, \delta_e, P_d]^\top$. Note that, the fault type is assumed to be detectable in the rudder runaway fault scenario.

To validate the new flight controller, a simulated flight test benchmark was designed (see. Fig. 2). In this figure, 'F' denotes failure, and $\triangle$ indicates an incremental quantity. The simulated flight test is a quite similar flight task to the trajectory tracking assignment carried out by Alwi and Edwards et al.[4], which enables the results in this paper to be compared to the results presented in [4, 5]. It should be noted that the altitude tracking control task would be switched into flight path angle command tracking mode at the 650^{th} second in order to mimic a landing process with fixed gliding slope (i.e.$\gamma = -3\,deg$).

All simulated flight tests in this paper are started from the same trim point with $V_{\mathrm{TAS}} = 133.8\,\mathrm{m/s}$, altitude$=600\,\mathrm{m}$ and $\delta_{\mathrm{ih}} = -0.65\,\mathrm{deg}$

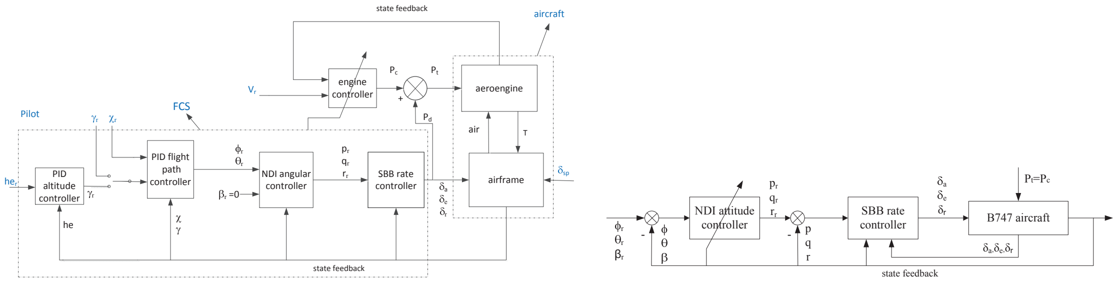

(a) Autopilot control architecture with four levels. (b) Attitude controller, engine separation or nominal case.

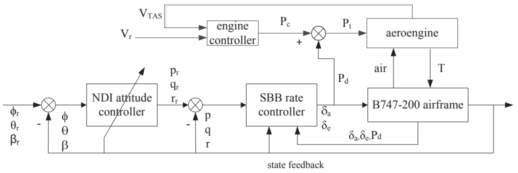

(c) Attitude controller, rudder runaway.

Fig. 1 Fault-tolerant controller configuration.

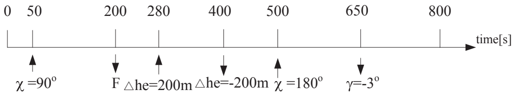

Fig. 2 Simulated flight test benchmark.

.

III. Attitude Controller and Preliminaries on Rate Control

A. Attitude Controller using NDI

In order to make the angular controller have a high level performance, the NDI control law from [5] is utilized to design an angular controller for the Boeing 747-200 aircraft. The reference commands for the inner rate loop are derived from the angular control loop as follows:

$$\begin{bmatrix} p_r \\ q_r \\ r_r \end{bmatrix} = \begin{bmatrix} 1 & \sin\phi\tan\theta & \cos\phi\tan\theta \\ 0 & \cos\phi & -\sin\phi \\ \frac{w}{\sqrt{u^2+w^2}} & 0 & \frac{-u}{\sqrt{u^2+w^2}} \end{bmatrix}^{-1} \left(\begin{bmatrix} \nu_\phi \\ \nu_\theta \\ \nu_\beta \end{bmatrix} - \begin{bmatrix} 0 \\ 0 \\ A_\beta \end{bmatrix} \right) \tag{1}$$

with

$$A_\beta = \frac{1}{\sqrt{u^2+w^2}} \left[\frac{-uv}{V^2} \left(A_x - g\sin\theta \right) + \left(1 - \frac{v}{V^2} \right) \left(A_y + g\sin\phi\cos\theta \right) - \frac{vw}{V^2} \left(A_z + g\cos\phi\cos\theta \right) \right]$$

where A_x, A_y, A_z are the accelerations along the body axes without the gravitational effects, and $\begin{bmatrix} \nu_\phi \ , \nu_\theta \ , \nu_\beta \end{bmatrix}^\top$ is the virtual angular command vector. The development of A_β is presented in

Sec. VI A. For further basic knowledge about NDI attitude controller design, the reader can refer to [19].

B. Rate Control Basis and Control Allocation

In order to introduce the control allocation more clearly, it is assumed, in this section, that an NDI rate controller has been designed for the aircraft according to [5]. The control inputs can be solved using the following formulation:

$$\mathbf{M}_{\mathrm{CA}} \cdot \mathbf{u} = \left\{ \frac{\mathbf{I}}{\frac{1}{2}\rho V^2 S} \left(\begin{bmatrix} \nu_p \\ \nu_q \\ \nu_r \end{bmatrix} + \mathbf{I}^{-1} \begin{bmatrix} p \\ q \\ r \end{bmatrix} \times \left(\mathbf{I} \begin{bmatrix} p \\ q \\ r \end{bmatrix} \right) \right) - \begin{bmatrix} bC_{l_{\mathrm{states}}} \\ \bar{c}C_{m_{\mathrm{states}}} \\ bC_{n_{\mathrm{states}}} \end{bmatrix} \right\} \tag{2}$$

with

$$\mathbf{M}_{\mathrm{CA}} = \begin{bmatrix} b & 0 & 0 \\ 0 & \bar{c} & 0 \\ 0 & 0 & b \end{bmatrix} \mathbf{M}_E \tag{3}$$

where $\begin{bmatrix} \nu_p \; \nu_q \; \nu_r \end{bmatrix}^\top$ are the virtual rate commands, $\mathbf{M}_{\mathrm{CA}}$ is the control allocation matrix, $\mathbf{M}_E$ is the control effectiveness matrix, $\mathbf{u}$ is the vector consisting of all the control inputs and $C_{l_{\mathrm{states}}}, C_{m_{\mathrm{states}}}, C_{n_{\mathrm{states}}}$ are the non-dimensional moments contributed by all of the current states. In the NDI rate controller, the unknown matrix $\mathbf{M}_E$ and the non-dimensional moments induced by the current states (i.e.$C_{l_{\mathrm{states}}}, C_{m_{\mathrm{states}}}, C_{n_{\mathrm{states}}}$) need to be identified in real-time [5]. One representative aerodynamic model identification method is the two-step identification method [20].

The Boeing 747-200 aircraft has 30 independent control inputs including 25 deflectable control surfaces, 4 engine pressure ratios (EPRs) and 1 flight gear (mode) input [1]. To simplify the control allocation logic, some of the aircraft inputs can be combined and the following 19 equivalent control variables can be used instead [4, 14, 21]:

$$\mathbf{u} = [\delta_a, \delta_{\mathrm{sp}}, \delta_e, \delta_{\mathrm{ih}}, \delta_r, \mathbf{P}_t, P_d]^\top \tag{4}$$

with

$$
\begin{aligned}
\delta_a &= [\delta_{\text{air}}, \delta_{\text{ail}}, \delta_{\text{aor}}, \delta_{\text{aol}}] \\
\delta_{\text{sp}} &= [(\delta_{\text{sp1}} + \delta_{\text{sp4}}), (\delta_{\text{sp2}} + \delta_{\text{sp3}}), (\delta_{\text{sp10}} + \delta_{\text{sp11}}), (\delta_{\text{sp9}} + \delta_{\text{sp12}})] \\
\delta_e &= [\delta_{\text{eir}}, \delta_{\text{eil}}, \delta_{\text{eor}}, \delta_{\text{eol}}] \\
\delta_r &= [\delta_{\text{ru}}, \delta_{\text{rl}}] \\
\mathbf{P}_t &= [P_{t_1}, P_{t_2}, P_{t_3}, P_{t_4}] \\
P_d &= \frac{1}{4}\left[(P_{t_1} - P_{t_4}) + (P_{t_2} - P_{t_3})\right]
\end{aligned}
\tag{5}
$$

with P_c the collective engine pressure ratio (EPR), P_d the differential EPR and $\mathbf{P}_t$ the vector consisting of four total EPRs. They are defined as follows:

$$
\begin{aligned}
P_c &= mean\left(\mathbf{P}_t\right) \\
P_{t_1} &= P_{t_2} = P_c + P_d \\
P_{t_3} &= P_{t_4} = P_c - P_d
\end{aligned}
\tag{6}
$$

Supposing that the matrix M_E in Eq. 2 has been identified and is currently available, an optimizer can be designed to solve the control allocation problem described by Eq. 2. However, the overall control effectiveness matrix and thus the control allocation operation may become unreliable during the transient period when structural model changes happen suddenly. In order to enhance the reliability of the control allocation operation in implementing the new control method, the M_E matrix used in this paper is simplified in further:

$$
M_E = \begin{bmatrix} \tilde{C}_{l\delta_a} & 0 & \tilde{C}_{l\delta_r} \\ 0 & \tilde{C}_{m\delta_e} & 0 \\ \tilde{C}_{n\delta_a} & 0 & \tilde{C}_{n\delta_r} \end{bmatrix}
\tag{7}
$$

with

$$\begin{aligned}
\tilde{C}_{l\delta_a} &= -C_{l\delta_{\mathrm{air}}} + C_{l\delta_{\mathrm{ail}}} - C_{l\delta_{\mathrm{aor}}} + C_{l\delta_{\mathrm{aol}}} - \\
&\quad C_{l\delta_{\mathrm{sp1}}} - \cdots - C_{l\delta_{\mathrm{sp4}}} + C_{l\delta_{\mathrm{sp9}}} + \cdots + C_{l\delta_{\mathrm{sp12}}} \\
\tilde{C}_{n\delta_a} &= -C_{n\delta_{air}} + C_{n\delta_{ail}} - C_{n\delta_{aor}} + C_{n\delta_{aol}} - \\
&\quad C_{n\delta_{\mathrm{sp1}}} - \cdots - C_{n\delta_{\mathrm{sp4}}} + C_{n\delta_{\mathrm{sp9}}} + \cdots + C_{n\delta_{\mathrm{sp12}}} \qquad (8) \\
\tilde{C}_{m\delta_e} &= C_{m\delta_{\mathrm{eir}}} + C_{m\delta_{\mathrm{eil}}} + C_{m\delta_{\mathrm{eor}}} + C_{m\delta_{\mathrm{eol}}} \\
\tilde{C}_{l\delta_r} &= C_{l\delta_{\mathrm{ru}}} + C_{l\delta_{\mathrm{rl}}} \\
\tilde{C}_{n\delta_r} &= C_{n\delta_{\mathrm{ru}}} + C_{n\delta_{\mathrm{rl}}}
\end{aligned}$$

Note that, Eq. 8 indicates that the control surfaces belonging to the same category would get equally distributed deflection commands in the control allocation process.

IV. SBB Rate Controller

In 1991, a singular perturbation theory based nonlinear control method was presented by Slotine et al.[22]. Then this control law was developed further by Hovakimyan et al.[15] to control a non-affine nonlinear system. In 2011, Falkena et al.[16] combined the singular perturbation theory with the backstepping technique, and developed an incremental type nonlinear backstepping control approach called the sensor based backstepping (SBB) approach. This Lyapunov function based control method can both guarantee the stability of the closed-loop system and avoid the requirement of full aerodynamic model information[16, 23].

In the SBB control approach, a singular perturbation theory based control approximation is adopted. In order to apply the singular perturbation theory, the system dynamics of the control plant need to have the time-scale separation property. In the aircraft system, the actuator system can be viewed as a subsystem cascaded to the body angular rate dynamic system. Since the actuator dynamics are much faster than the body rate dynamics, the time-scale separation property of the aircraft is guaranteed. This allows us to use the SBB control approach to design a body angular rate controller for the Boeing 747-200 aircraft model. The structure of the rate controller is shown in the first level of Fig. 1(a).

A. Sensor Based Backstepping Rate Control

The following expression holds for the body angular rate aerodynamics:

$$\begin{bmatrix} \dot{p} \\ \dot{q} \\ \dot{r} \end{bmatrix} = -\left\{ \mathbf{I}^{-1} \left(\begin{bmatrix} p \\ q \\ r \end{bmatrix} \times \left(\mathbf{I} \begin{bmatrix} p \\ q \\ r \end{bmatrix} \right) \right) - \frac{1}{2}\rho V^2 S \cdot \mathbf{I}^{-1} \begin{bmatrix} bC_{l_{\text{states}}} \\ \bar{c}C_{m_{\text{states}}} \\ bC_{n_{\text{states}}} \end{bmatrix} \right\} + \frac{1}{2}\rho V^2 S \cdot \mathbf{I}^{-1}\mathbf{M}_{\text{CA}} \cdot \mathbf{u} \tag{9}$$

Rewrite Eq. 9, a simplified formulation of the aircraft motion equations is derived:

$$\dot{\mathbf{x}} = f\left(\mathbf{x}\right) + \mathbf{g} \cdot \mathbf{u} \tag{10}$$

with

$$\mathbf{x} = \begin{bmatrix} p \ q \ r \end{bmatrix}^{\top} \tag{11a}$$

$$\mathbf{y}_r = \begin{bmatrix} p_r \ q_r \ r_r \end{bmatrix}^{\top} \tag{11b}$$

$$\mathbf{e} = \mathbf{x} - \mathbf{y}_r \tag{11c}$$

$$\mathbf{g} = \frac{1}{2}\rho V^2 S \cdot \mathbf{I}^{-1} M_{\text{CA}} \tag{11d}$$

$$f\left(\mathbf{x}\right) = -\mathbf{I}^{-1} \left(\begin{bmatrix} p \\ q \\ r \end{bmatrix} \times \left(\mathbf{I} \begin{bmatrix} p \\ q \\ r \end{bmatrix} \right) \right) + \frac{1}{2}\rho V^2 S \cdot \mathbf{I}^{-1} \begin{bmatrix} bC_{l_{\text{states}}} \\ \bar{c}C_{m_{\text{states}}} \\ bC_{n_{\text{states}}} \end{bmatrix} \tag{11e}$$

In order to design a single-loop body rate backstepping controller, the control Lyapunov function V is chosen as follows:

$$\begin{aligned} V\left(\mathbf{e}\right) &= \frac{1}{2}\mathbf{e}^2 + \frac{1}{2}\mathbf{k}\lambda^2 \\ \dot{V}\left(\mathbf{e}\right) &= \mathbf{e}\dot{\mathbf{e}} + \mathbf{k}\lambda\mathbf{e} \end{aligned} \tag{12}$$

with $\mathbf{e} = \mathbf{e}\left(t\right)$, $\mathbf{k}$ a diagonal matrix of controller gains, and $\lambda = \int_0^t \mathbf{e} dt$ an integral term introduced to remove the tracking errors caused by the internal dynamics. Note that $\dot{\lambda} = \mathbf{e}$ holds.

Using Eq. 11c, the following expression can be derived for the desired state of the control system:

$$\mathbf{e} = \mathbf{x}_{des} - \mathbf{y}_r \tag{13}$$

$$\dot{\mathbf{e}} = \dot{\mathbf{x}}_{des} - \dot{\mathbf{y}}_r \tag{14}$$

Substituting Eq. 14 into Eq. 12 results in:

$$\dot{V}\left(\mathbf{e}\right) = \mathbf{e}\dot{\mathbf{e}} + \mathbf{k}\lambda\mathbf{e} = \mathbf{e}\left(\dot{\mathbf{x}}_{des} - \dot{\mathbf{y}}_r + \mathbf{k}\lambda\right) \tag{15}$$

To stabilize this system, $\dot{\mathbf{x}}_{des}$ can be selected as:

$$\begin{aligned} \dot{\mathbf{x}}_{des} &= -\,\mathbf{c}\mathbf{e} + \dot{\mathbf{y}}_r - \mathbf{k}\lambda \\ &-\,\mathbf{c}\left(\mathbf{x} - \mathbf{y}_r\right) + \dot{\mathbf{y}}_r - \mathbf{k}\lambda \end{aligned} \tag{16}$$

with $\mathbf{c}$ a positive diagonal matrix to stabilize the system. This yields the desired system:

$$\dot{\mathbf{e}} = -\mathbf{c}\left(\mathbf{x} - \mathbf{y}_r\right) \tag{17}$$

The following notation is defined for later usage:

$$\mathbf{u}_{\text{red}} = \mathbf{M}_{\text{CA}} \cdot \mathbf{u} \tag{18}$$

with $\mathbf{u}_{\text{red}}$ a three dimensional vector denoting the equivalent inputs. After substituting Eq. 18 into Eq. 11d, the SBB controller for Eq. 10 can be derived according to [15, 16, 24]:

$$\begin{aligned} \epsilon\dot{\mathbf{u}}_{\text{red}} &= -sgn\left(\frac{\partial\dot{\mathbf{x}}}{\partial\mathbf{u}_{\text{red}}}\right)\left[\dot{\mathbf{x}} - \dot{\mathbf{x}}_{des}\right] \\ &= -sgn\left(\frac{\partial\dot{\mathbf{x}}}{\partial\mathbf{u}_{\text{red}}}\right)\left[\dot{\mathbf{x}} + \mathbf{c}\left(\mathbf{x} - \mathbf{y}_r\right) - \dot{\mathbf{y}}_r + \mathbf{k}\lambda\right] \end{aligned} \tag{19}$$

where ϵ is a tuning parameter with a small positive value (i.e. $0<\epsilon \ll 1$). From Eq. 9, the following formulation can be obtained:

$$-sgn\left(\frac{\partial\dot{\mathbf{x}}}{\partial\mathbf{u}_{\text{red}}}\right) = -sgn\left(\frac{1}{2}\rho V^2 S \cdot \mathbf{I}^{-1}\right) \tag{20}$$

Substituting Eq. 20 into Eq. 19, the control inputs are computed as follows:

$$\dot{\mathbf{u}}_{\text{red}} = -\frac{1}{\epsilon} sgn\left(\frac{1}{2}\rho V^2 S \cdot \mathbf{I}^{-1}\right)\left[\dot{\mathbf{x}} + \mathbf{c}\left(\mathbf{x} - \mathbf{y}_r\right) - \dot{\mathbf{y}}_r + \mathbf{k}\lambda\right] \tag{21}$$

Using integration, the equivalent control input $\mathbf{u}_{red}$ can be calculated as follows:

$$\mathbf{u}_{\text{red}_k} = \mathbf{u}_{\text{red}_{k-1}} + \int_{(k-1)T}^{kT} \dot{\mathbf{u}}_{\text{red}} \cdot dt \tag{22}$$

According to Eq. 18, the control input $\mathbf{u}$ can be solved using a control allocation algorithm if $\mathbf{M}_{\text{CA}}$ is available.

Note that, the objective of this paper is to present a flight controller which does not require an online aerodynamic model. However, Eq. 18 is still dependent on the partial aerodynamic model (i.e. control effectiveness matrix $\mathbf{M}_{\text{CA}}$) identified in real-time. In order to remove this online model dependency, a fixed $\mathbf{M}_{\text{CA}}$ matrix is usually used (see. [4]). The drawback of doing so is that the optimality of the control allocation can not be guaranteed since it is directly determined by the accurate knowledge of $\mathbf{M}_{\text{CA}}$. In this paper, a fixed $\mathbf{M}_{\text{CA}}$ is assumed to be available at a trim point.

To simplify the implementation of the controller, the requirement of the control allocation is removed from the design procedures. Remember that the control surfaces have been categorized into 3 groups (see. Eq. 8). In each group, a control surface is chosen as the representative control input. Consequently, a representative control input vector $\mathbf{u}_{\text{rep}} = \left[\delta_{1_{\text{rep}}}, \delta_{2_{\text{rep}}}, \delta_{3_{\text{rep}}}\right]$ can be derived with $\delta_{1_{\text{rep}}}$, $\delta_{2_{\text{rep}}}$, $\delta_{3_{\text{rep}}}$ a representative control surface deflection selected from each category respectively. For example, the representatives can be selected as follows: $\delta_{1_{\text{rep}}} = \delta_{\text{ail}}$, $\delta_{2_{\text{rep}}} = \delta_{\text{eil}}$ and $\delta_{3_{\text{rep}}} = \delta_{\text{ru}}$ (or $\delta_{3_{\text{rep}}} = P_d$). The control allocation matrix $\mathbf{M}_{\text{CA}_{\text{rep}}}$ can be calculated from the aforementioned fixed matrix $\mathbf{M}_{\text{CA}}$ using Eq. 7. This means there exists the following assumption at this place:

$$\mathbf{M}_{\text{CA}_{\text{rep}}} \cdot \mathbf{u}_{\text{rep}} \approx \mathbf{M}_{\text{CA}} \cdot \mathbf{u} \tag{23}$$

After substituting Eq. 23 into Eq. 11d, the SBB controller can be redesigned for the system Eq. 10. Consequently, the term $\frac{\partial \dot{\mathbf{x}}}{\partial \mathbf{u}_{\text{red}}}$ in Eq. 19 and Eq. 20 should be replaced by $\frac{\partial \dot{\mathbf{x}}}{\partial \mathbf{u}_{\text{rep}}}$, and Eq. 20 becomes:

$$-sgn\left(\frac{\partial \dot{\mathbf{x}}}{\partial \mathbf{u}_{\text{rep}}}\right) = -sgn\left(\frac{1}{2}\rho V^2 S \cdot \mathbf{I}^{-1}\mathbf{M}_{\text{CA}_{\text{rep}}}\right) \tag{24}$$

While, Eq. 21 becomes:

$$\dot{\mathbf{u}}_{\text{rep}} = -\frac{1}{\epsilon} sgn\left(\frac{1}{2}\rho V^2 S \cdot \mathbf{I}^{-1}\mathbf{M}_{\text{CA}_{\text{rep}}}\right)\left[\dot{\mathbf{x}} + \mathbf{c}\left(\mathbf{x} - \mathbf{y}_r\right) - \dot{\mathbf{y}}_r + \mathbf{k}\lambda\right] \tag{25}$$

Subsequently, $\mathbf{u}_{\text{rep}}$ can be calculated using Eq. 22. In calculating $sgn\left(\frac{1}{2}\rho V^2 S \cdot \mathbf{I}^{-1}\mathbf{M}_{\text{CA}_{\text{rep}}}\right)$, the same method as that used in [15] is adopted. That is, only the sign of the diagonal elements of the matrix (in the bracket) are used in designing the body angular rate controller.

The configuration of the SBB rate controller is summarized in Fig. 3. 'TA' is the acronym of tuning algorithm (TA), and τ represents the time delay between the achieved control input $\mathbf{u}$ and the controller output $\mathbf{u}_{\text{des}}$, which is caused by the dynamics, saturation or failures of the actuators. It also should be noted that the SBB method contains a tuning parameter called time-scale constant parameter denoted by ϵ, which helps to simplify the tuning process of other control gains.

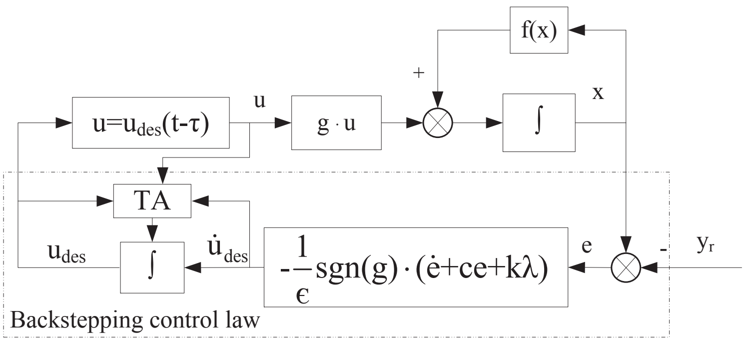

Fig. 3 flow chart of the SBB inner-loop controller.

B. Command Filter and Integration Saturation

A command filter is designed to regulate the given reference commands in order to enhance handling qualities of the closed-loop aircraft system. By regulating the reference command into an achievable command, the command filter can play a crucial role in preventing the aircraft from leaving the safe flight envelope.

The windup effect associated with the integrator needs to be removed. The saturation effect may become even severe when some structural failures happen to the control surfaces or there exists a big time-delay on the control effector (e.g. the propulsion system). In this paper, a tuning algorithm (TA) block was designed to prevent the closed-loop system from integral windup. It uses the discrepancy information between the achieved control inputs $\mathbf{u}$ and the integrator outputs $\mathbf{u}_{\text{des}}$. As shown in Fig. 3, the TA block will compare $\mathbf{u}_{\text{des}}$ with $\mathbf{u}$ and the saturated position limits. If the actuators are saturated or the changing rate of $\mathbf{u}$ is far more slower than $\mathbf{u}_{\text{des}}$, the integration operation, which intends to increase the difference (determined by the sign of $\dot{\mathbf{u}}_{\text{des}}$), will be skipped in the current time instant.

V. Results and Analysis

Up to now, a hybrid NDI/SBB angular control approach has been developed in Sec. III and Sec. IV. In order to allow the aircraft to track the flight path commands (χ_r, γ_r and V_{TASr}), the airspeed controller and the flight path angle controller are designed to complete the autopilot designing. Cooperative control of flight path angle and airspeed can be achieved using the total

Table 1 Control input units and maximum values

Control	Unit	Min	Max	Full hydraulic rate	Half hydraulic rate
δ_{ai}	deg	-20	20	+40/-45 deg/s	+27/-35 deg/s
δ_{ao}	deg	-25	15	+45/-55 deg/s	+22/-45 deg/s
δ_e	deg	-23	17	±37 deg/s	+30/-26 deg/s
δ_r	deg	-25	25	±50 deg/s	±40 deg/s
δ_{ih}	deg	-12	3	±0.2-±0.5 deg/s	±0.1-±0.25deg/s
$\delta_{sp1-4}, \delta_{sp9-12}$	deg	0	45	+75 deg/s	0
δ_{sp5} δ_{sp8}	deg	0	20	+75 deg/s	0
δ_{sp6} δ_{sp7}	deg	0	20	+25 deg/s	0
P_{t1-4}	-	0	1.62	± 0.2 s^{-1}	± 0.2 s^{-1}

energy control principles (TECS) [25] or the model-based dynamic inversion method [26], which takes into account couplings of flight dynamics. Both of these two methods have the potential to enhance the airspeed and the flight path control performance. However, the focus of this paper is limited to validating the proposed hybrid NDI/SBB angular controller, which does not require any online model information. In this paper, a flight path controller is designed using the regular PID control laws, where γ, χ are regulated independently (see. Fig. 1(a)). In addition, an independent airspeed controller is designed using PID, where P_c are chosen as control inputs. It should be noted that the flight path control-loop does not require the adaptation for changes in aerodynamic forces (e.g. lift, drag and side-force).

The overall flight path controller will be validated using the aerodynamic model of Boeing 747-200 aircraft. It will be firstly evaluated for the nominal case and then evaluated using rudder runaway and right engine separation failures introduced in Sec. II. Eq. 8 and Eq. 6 are implemented to realize the control allocation (i.e. equally distributed).

A. Command Filter Setup and Actuator Working Range

The actuators of the control surfaces are modeled with saturation limits and deflection rate limits (see Table 2). In this paper, a command filter developed in [27] would be utilized. This filter has an adjustable natural frequency ω_n and damping ratio ζ. The scheduling limits on the body

Table 2 Command filter parameters and command ranges

Commands	Unit	Min	Max	ω_n	ζ
p	rad	-0.2	0.2	3 rad/s	1
q	rad	-0.2	0.2	3 rad/s	1
r	rad	-0.1	0.1	1.2 rad/s	1
ϕ	deg	-20	20	2.5 rad/s	1
θ	deg	-12	12	2.5 rad/s	1
β	deg	-20	20	2.5 rad/s	1

Table 3 PI parameters of the outer loop PID controllers

Channel	$\chi \leftarrow \phi$	$\gamma \leftarrow \theta$	H $\leftarrow \gamma$	$V_{TAS} \leftarrow P_c$
Proportional gain	2	0.7	0.139	0.02
Integral gain	0.1	0.3	0	0.0025

angular rate commands and the attitude angular commands are listed in Table 2.

B. Outer Loop Controller Parameters

As mentioned in Sec.II, a PID controller has been designed to control V_{TAS}, χ, γ and H. The PID parameters of these outer loop controller are listed in Table 3.

C. Validation Results of the Nominal Aircraft

The proposed hybrid NDI/SBB attitude controller (see Fig. 1(b))is tested by flying the Boeing 747-200 aircraft in the nominal state (i.e. fault-free case). The numerical simulation results are plotted in Fig.4-15. The idea of a fault-free test of the controller is to show the capability of the proposed controller. The chosen values of the controller parameters are listed in Table 4.

Figs.4-15 give the validation results of the controller under the nominal flight case. The designed

Table 4 Hybrid NDI/SBB attitude controller parameters, $\epsilon = 0.15$, nominal/engine separation

Channel	proportion	integration
Angular control	$[1, 1, 2]$	$[0, 0.02, 0.1]$
Body rate control	$[0.1, 0.2, 0.1]$	$[0, 0, 0]$

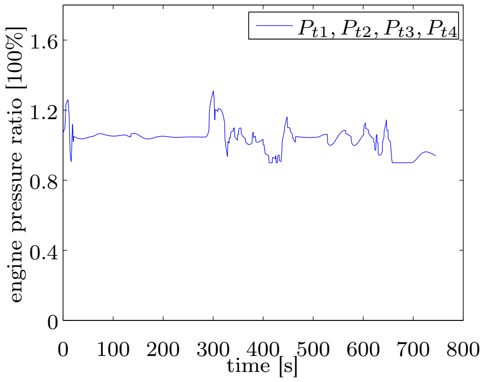

Fig. 4 Engine Pressure Ratios, nominal.

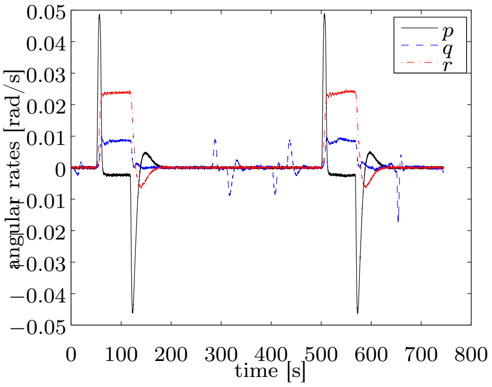

Fig. 5 Actual angular rates, nominal.

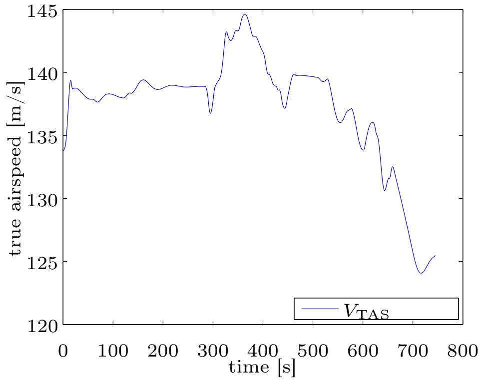

Fig. 6 True airspeed, nominal.

control command sequences (see Fig. 2) were fed to the autopilot. Fig. 4 shows the changing history of the EPRs, and the EPRs are regulated to keep the true airspeed between 142 m/s and 122 m/s

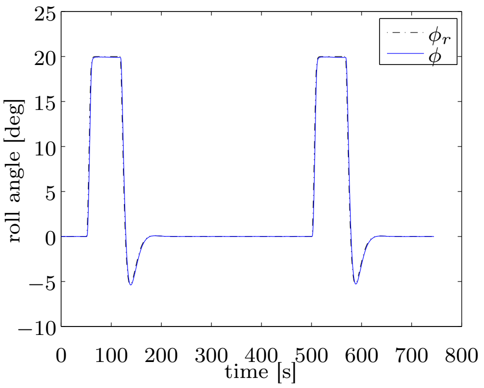

Fig. 7 Roll angle, nominal.

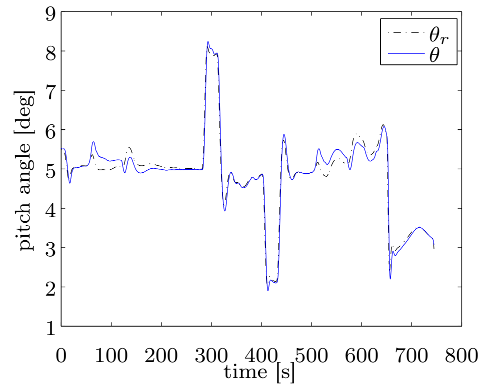

Fig. 8 Pitch angle, nominal.

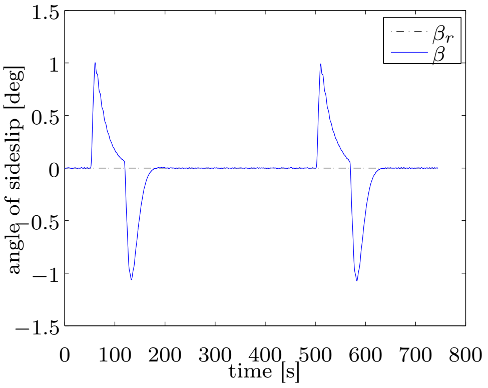

Fig. 9 Angle of sideslip, nominal.

throughout the simulation (see. Fig. 6).

The body angular rate changes are illustrated in Fig. 5, and the tracking performance of the

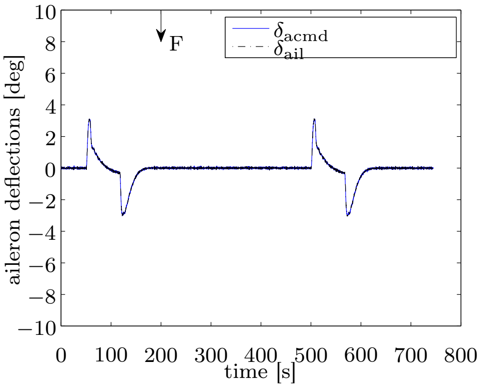

Fig. 10 Commanded and actual aileron deflections, nominal.

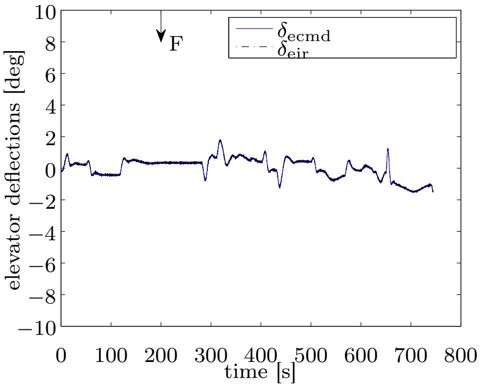

Fig. 11 Commanded and actual elevator deflections, nominal.

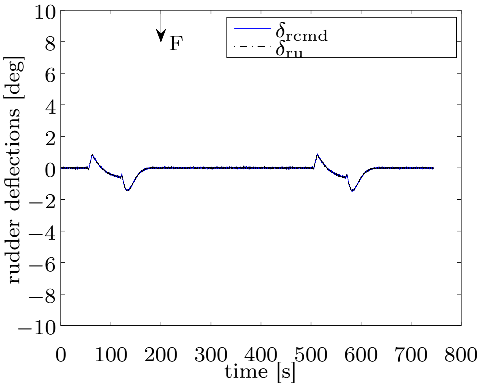

Fig. 12 Commanded and actual rudder deflections, nominal.

angular commands is depicted in Fig.7-9. As can be seen from Figs.7-9, the inner component (i.e. attitude controller) of the autopilot controller enables the aircraft to closely track the attitude

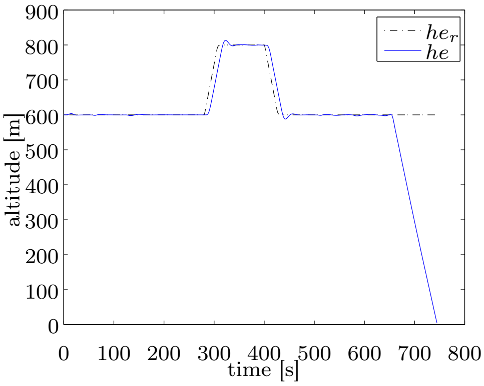

Fig. 13 Altitude, nominal.

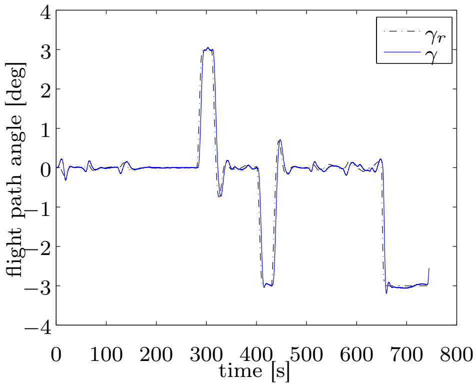

Fig. 14 Flight path angle, nominal.

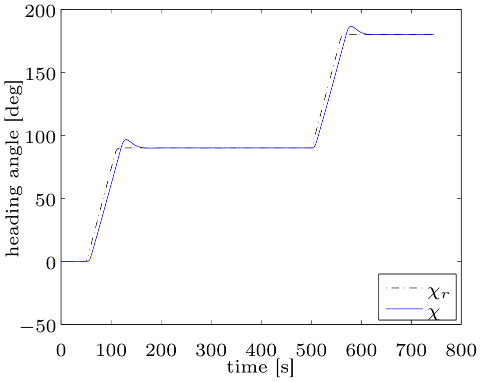

Fig. 15 Heading angle, nominal.

commands.

Figs.10-12 show the commanded and actual deflections of aileron, elevator and rudder respec-

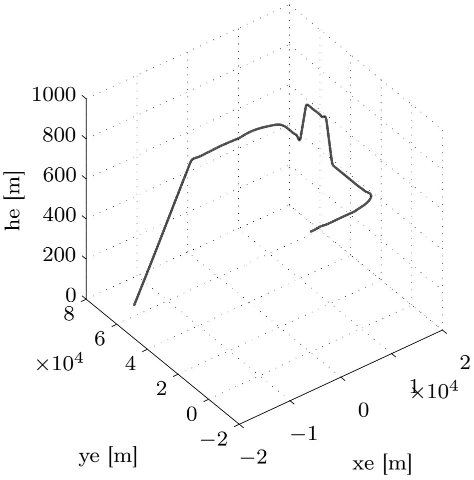

Fig. 16 Three-dimensional trajectory, nominal.

tively. Specifically, Fig. 10 shows the commanded and actual aileron deflections. As can be seen from them, the actual control surface deflections highly match the commanded deflections, which also means there exists no integration saturation.

Finally, the tracking performance in the flight path control level are illustrated in Fig.13-15. The tracking commands of he, γ and χ are well followed. In all simulation experiments of this paper, the aircraft is in the altitude control mode before the 650^{th} second. And the altitude control loop is switched into the flight path angle control mode at the 650^{th} second. The three-dimensional trajectory is shown in Fig. 16.

D. Validation Results using Fault Scenarios

In the first simulation experiment, the hybrid attitude controller shown in Fig. 1(b) is evaluated. The controller parameters have already been listed in Table 4.

The simulated flight test results of the right engine separation scenario are plotted in Figs.17-28. The engine separation failure is triggered at the 200^{th} second (see. Fig. 31).

Fig. 17 shows the EPRs of the remaining working engines (engine ♯1 and engine ♯2). The EPRs are adjusted to keep V_{TAS} around 140 m/s (see Fig. 19), and try to slow down the airspeed before landing. It should be noted that the true airspeed shows a decrease fight right after 280th second

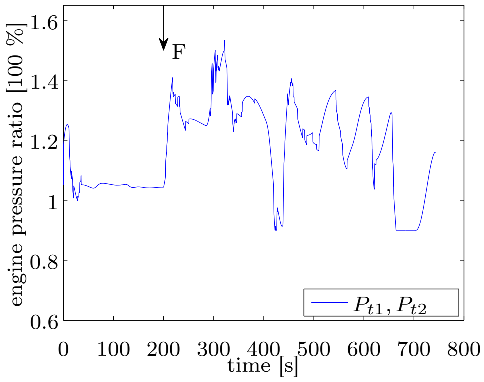

Fig. 17 Engine Pressure Ratios, engine separation.

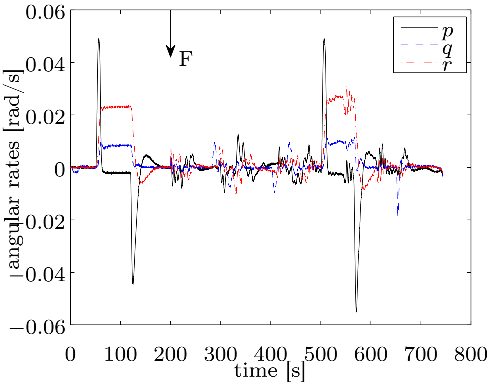

Fig. 18 Actual angular rates, engine separation.

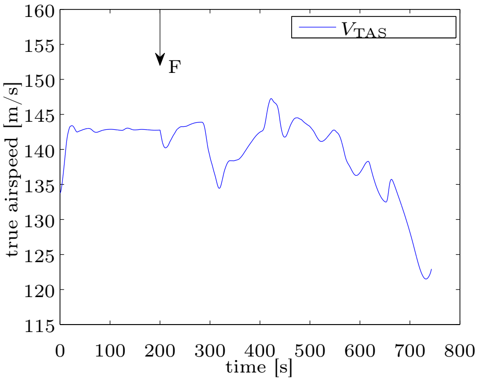

Fig. 19 True airspeed, engine separation.

due to the inadequate supply of power during the climbing. The changing histories of the actual values of p q and r are illustrated in Fig. 18, and they show stability character even under the

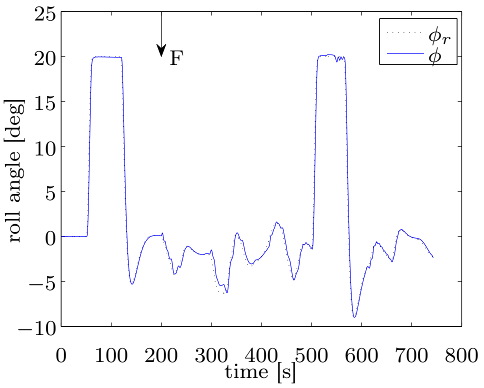

Fig. 20 Roll angle, engine separation.

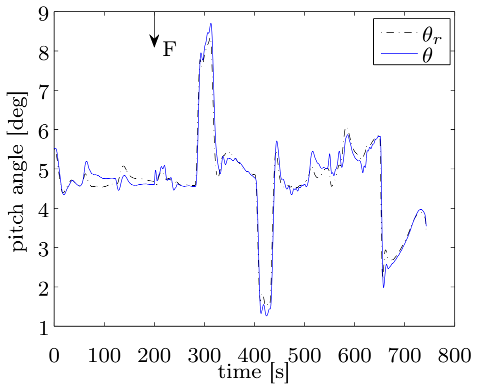

Fig. 21 Pitch angle, engine separation.

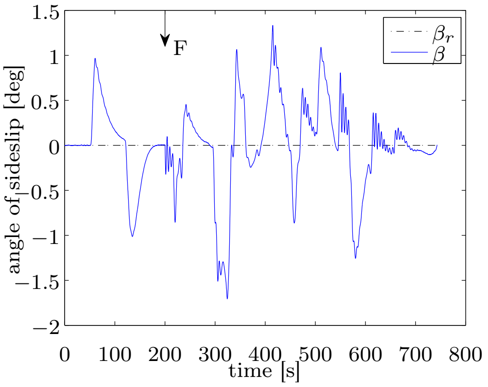

Fig. 22 Angle of sideslip, engine separation.

engine separation failure. During the coordinate turning (see.Fig.20, from 50s to 120s), p and r are regulated cooperatively. While, they are all kept around zero during level straight flight.

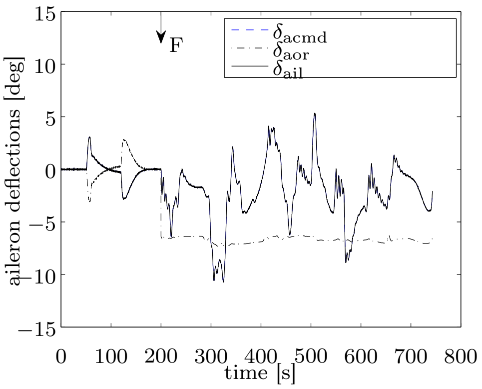

Fig. 23 Commanded and actual aileron deflections, engine separation.

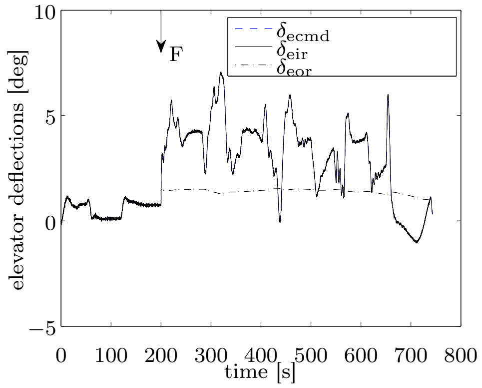

Fig. 24 Commanded and actual elevator deflections, engine separation.

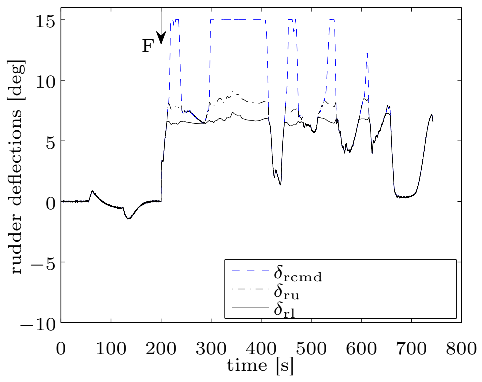

Fig. 25 Commanded and actual rudder deflections, engine separation.

The attitude command tracking performance of the proposed controller is depicted in Fig.20-22. The figures clearly show that ϕ and θ have a zero tracking error , β will keep smaller than 1.8

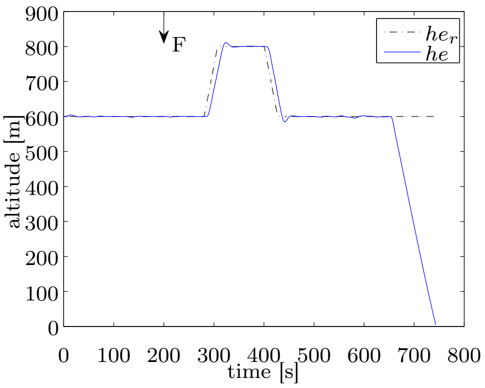

Fig. 26 Altitude, engine separation.

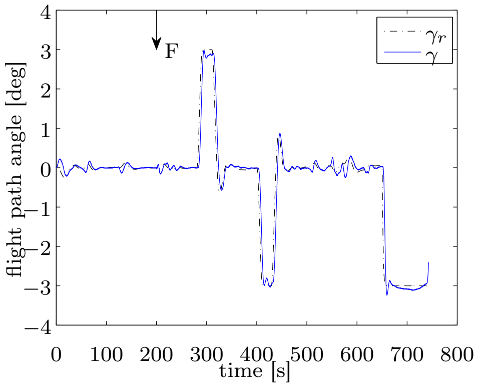

Fig. 27 Flight path angle, engine separation.

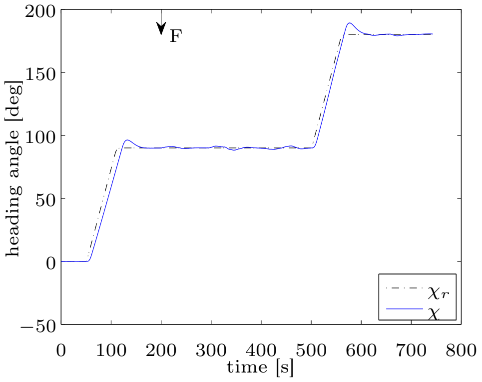

Fig. 28 Heading angle, engine separation.

degree. The tracking error of β decreases slowly, this is because the remaining control authority of the rudders are quite limited. This is due to the fact that a relatively large part of the working

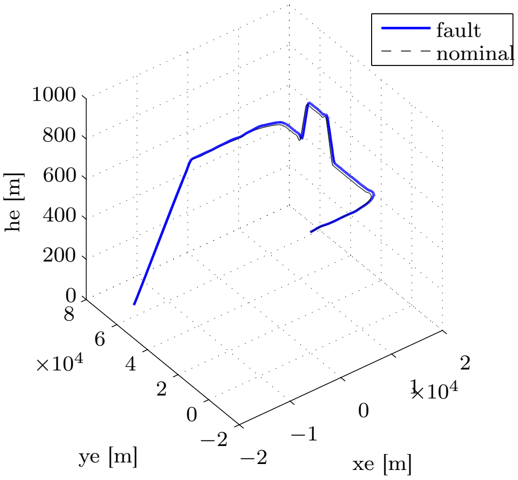

Fig. 29 Three-dimensional trajectory, engine separation.

range of the rudders has been occupied by the requirement of compensating the yawing moment produced by the right wing engine separation as can be seen in Fig. 25.

The changing history of the commanded and actual (under the physical limitations) control surface deflections are depicted by Figs.23-25. The control surface deflections of aileron, elevator and rudder are plotted separately. As can be seen from Figs.23-24, δ_{eil} δ_{eor} and δ_{aor} are not active/responding under this failure scenario, which is in consistent with the description of the engine separation scenario given by Sec. II. In Fig. 25, there exists large difference between the commanded and the actual rudder deflection after the $200th$ second, which indicates that the rudder often (e.g. $200th$ $400th$ seconds) needs to work in a saturated state.

Figs.26-28 provide the records of the command tracking performance in the flight path level. The heading angle command as well as the altitude command has been well tracked. It should be mentioned that the aircraft is under the altitude control mode before the 650^{th} second. Therefore, the flight path angle controller is acting as an inner-loop controller, which is thus not necessary to remove the transient tracking errors. As indicated by [4, 5], the climbing capability would be greatly reduced in the engine separation scenario. That is, a deep climbing becomes not achievable without airspeed loss even when the engine thrust is saturated. In our simulation, the aircraft climbs from $H = 600m$ to $H = 800m$ in about 50 seconds. The airspeed loss is about $10m/s$, which is the price

Table 5 Hybrid NDI/SBB attitude controller parameters, $\epsilon = 0.35$, rudder runaway

Chanel	proportion	integration
Angular control	$[1, 1, 1]$	$[0.12, 0.12, 0.02]$
Body rate control	$[2, 1, 0.1]$	$[0, 0, 0]$

paid for the climbing. Finally, the three-dimensional trajectory is shown in Fig. 29, where the curve for the nominal case is borrowed from Fig. 16.

The hybrid NDI/SBB attitude controller is validated using the rudder runaway scenario. As shown in Fig. 1(c), differential thrust is utilized to compensate the yawing moment induced by the failure. The controller parameters are tabulated in Table 5. The rudder runaway test of the hybrid controller is also performed for showing the adaptation ability of the proposed controller when the aircraft model changes suddenly.

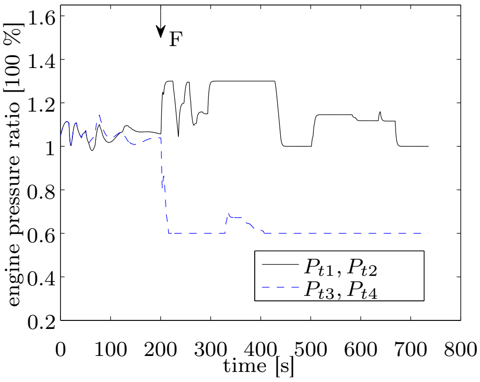

Fig. 30 Engine Pressure Ratios, rudder runaway.

The validation results of the hybrid NDI/SBB attitude controller in the rudder runaway case are plotted in Figs.30-43. The changes of the total EPRs ($\mathbf{P}_t$) are shown in Fig. 30, and all of them reach saturation limits just after the rudder runaway failure occurs. The true airspeed is controlled by the collective thrust P_c, and its changing history is plotted in Fig. 32. V_{TAS} ranges from 135 m/s to 160 m/s. This is made possible by limiting the upper bound of the total thrust P_t when the rudder is stuck to the left limit. The differential thrust P_d is regulated to actively generate yawing moment once needed by the flight control mission.

As shown in Fig. 31, the rudder runaway failure occurs at the 200^{th} second, and it produces

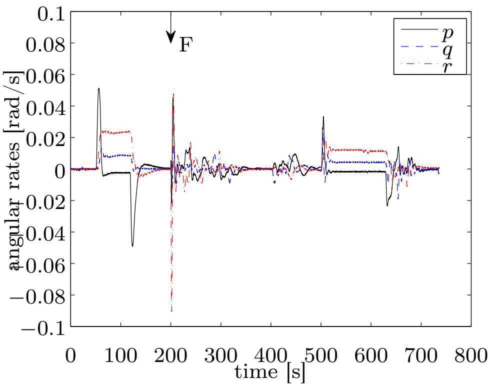

Fig. 31 Actual angular rates, rudder runaway.

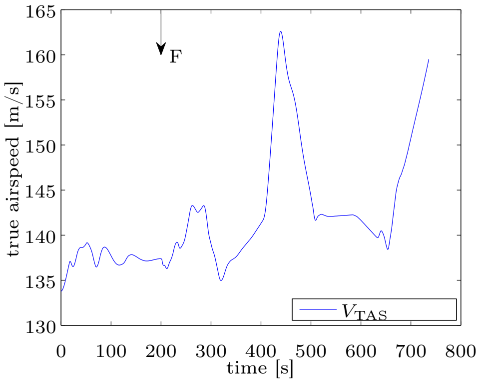

Fig. 32 True airspeed, rudder runaway.

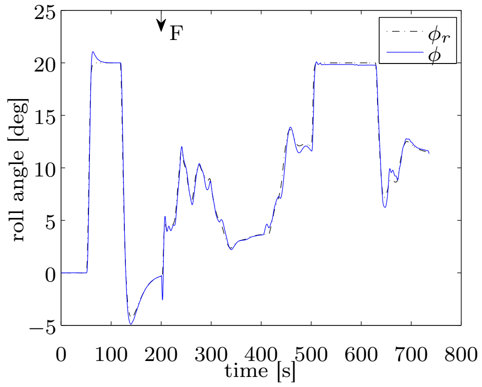

Fig. 33 Roll angle, rudder runaway.

a big influence on the body angular rates in a short transient period. The yawing rate r shows a spike around the 200^{th} second. This is caused by two factors: the influence from the stuck rudder

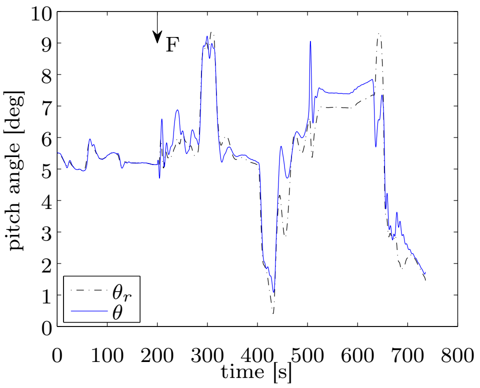

Fig. 34 Pitch angle, rudder runaway.

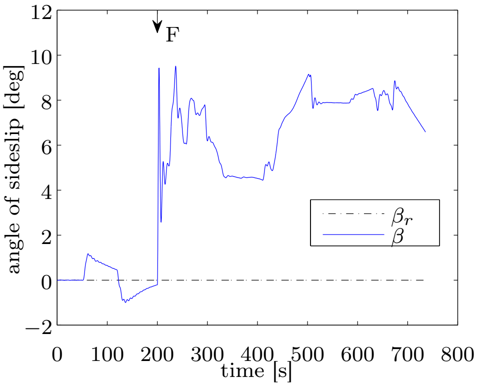

Fig. 35 Angle of sideslip, rudder runaway.

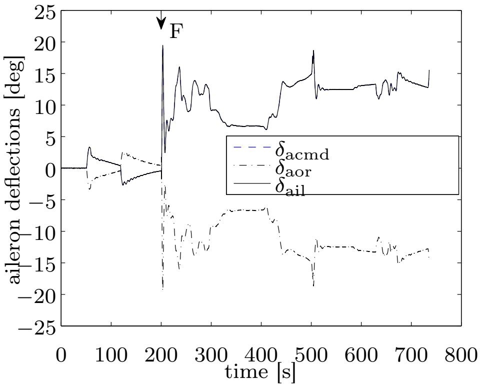

Fig. 36 Commanded and actual aileron deflections, rudder runaway.

and the control reaction. Specifically, it is the rudder failure that makes the yawing rate r reaches $-0.1\ rad/s$. While, it is the control reaction (using the differential thrust) as well as the side-force

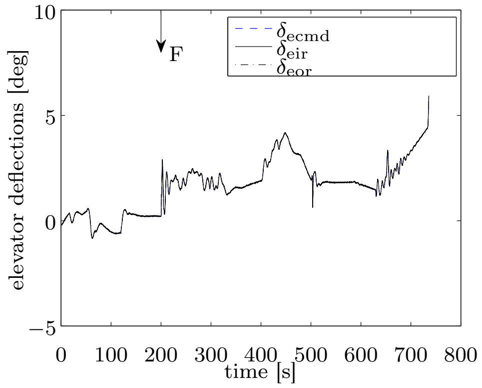

Fig. 37 Commanded and actual elevator deflections, rudder runaway.

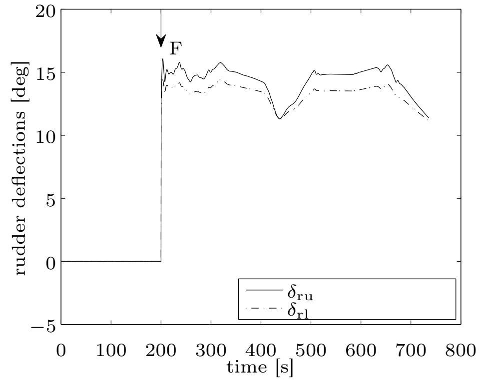

Fig. 38 Actual rudder deflections limited by actuator dynamics, rudder runaway.

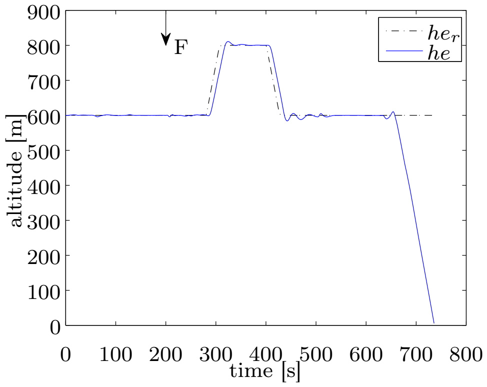

Fig. 39 Altitude, rudder runaway.

counteraction effect induced by the instantaneous nonzero β that makes r approach $+0.05\ rad/s$.

The angular command tracking performance of the hybrid controller are illustrated in Figs.33-

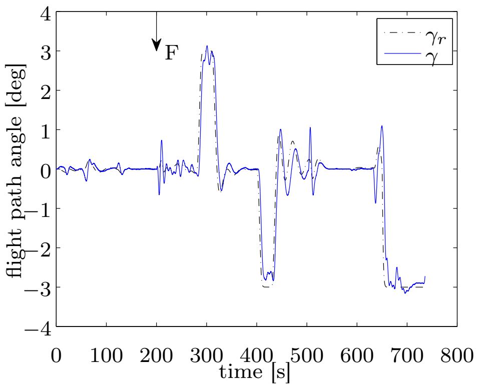

Fig. 40 Flight path angle, rudder runaway.

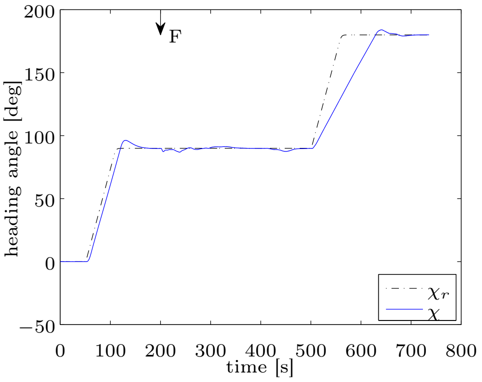

Fig. 41 Heading angle, rudder runaway.

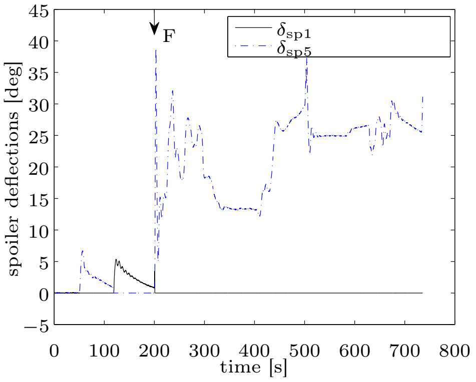

Fig. 42 Spoiler deflection, rudder runaway.

35. ϕ and θ have nearly a zero tracking error, and β keeps smaller than $9.2deg$ and it varies with time. The deterioration in the tracking performance of β is caused by the rudder runaway failure

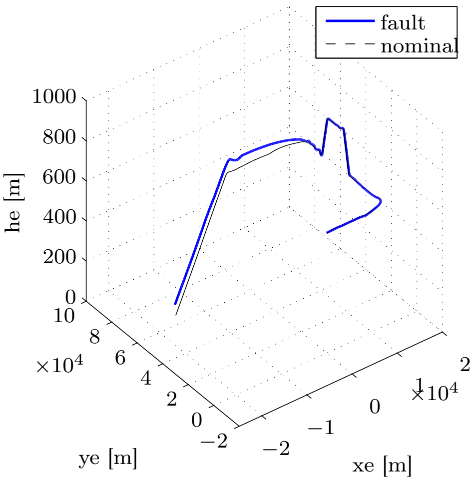

Fig. 43 Three-dimensional trajectory, rudder runaway.

scenario, which nearly uses up all the control authority of the differential thrust. The non-zero tracking errors of β is comparable to those presented in [5] under the same fault scenario.

Figs.36-37 provide the changing history of the commanded and actual (limited by the actuator dynamics and failures) control surface deflections for the roll and pitch channel respectively. In Fig. 38, the actual control surface deflections of the stuck rudders are plotted. It should be noted that the deflection angles of the rudders vary although they are stuck to the left limit after the $200th$ second (see. Fig. 38). The changes in deflection angles of rudders are caused by the fact that the aerodynamic blow-down has been taken into account by the RECOVER model. This has been confirmed by the fact that a correlation can be observed between (higher) airspeed and (lower) deflection angle (see. [5]).

Figs.39-41 show that he, γ and χ are closely tracking their own reference command respectively. It also should be noted that the autopilot controller is switched from altitude controller into flight path hold controller at the 650^{th} second. That is, the aircraft is controlled in the altitude control mode during the first 650 seconds. Therefore, it is reasonable that the tracking error of γ appears to be relatively large in a few transient periods.

The changing history of the deflection angles of spoilers are depicted in 42. The spoiler is assisting the ailerons to realize the control in the roll channel. Finally, the three-dimensional trajectory is shown in Fig. 43. Again, the curve for the nominal case is borrowed from Fig. 16. It can be observed from Fig. 43 that a wider turn is needed by the post-failure aircraft. Though the roll angle is still kept around $20deg$, the sideslip angle is relatively big, which explains why the turn becomes wider.

VI. Conclusions

This paper has presented a new autopilot flight controller with four levels of control loops. The core of the autopilot flight controller is a hybrid NDI/SBB attitude control unit, which does not require real-time full aircraft model information. The controller is applied to the RECOVER model of the Boeing 747-200 aircraft, and evaluated using rudder runaway and EL AL 1862 benchmark fault scenarios developed by the GARTEUR FM-AG 16. The numerical simulation results show that the proposed hybrid NDI/SBB attitude controller can keep the safety of the aircraft even when the aforementioned failures occur, and can ensure a zero tracking error performance for roll angle and pitch angle commands as long as the aircraft is still controllable with the remaining valid control surfaces.

This paper uses the singular perturbation theory based sensor based backstepping (SBB) control approach, and extends its application to the body angular rate control of the Boeing 747-200 aircraft with special concern on sudden model-changes. In addition, this SBB rate controller is combined with the NDI attitude controller and the PID flight path controller, and an autopilot flight controller has been synthesized. In the controller design, the control allocation problem is simplified by bounding a number of the control surfaces into a group. In addition, a second order command filter is adopted to enhance the handling quality. Compared with the classic adaptive nonlinear dynamic inversion (ANDI) control approach or adaptive backstepping control law, the hybrid NDI/SBB attitude control setup needs less online model information. However, for the SBB body angular rate control approach, more research is needed into investigating the effects of time-delay in the actuator dynamics, as well as the measurement noise, before the method can be applied in real-world applications. For example, the influence from the engine response, which has a significant time-delay in real life (especially in low thrust levels), needs to be further investigated.

Appendix

A. Calculate β related NDI term

From the flight dynamics, the sideslip angle is defined as:

$$\beta = \arcsin\left(\frac{v}{V}\right) \tag{26}$$

with

$$V = \sqrt{u^2 + v^2 + w^2} \tag{27}$$

By taking the time derivatives of β, Eq. 26 becomes:

$$\begin{aligned} \dot{\beta} &= \frac{\dot{v}V - v\dot{V}}{V\sqrt{V^2 - v^2}} = \frac{\dot{v}}{\sqrt{V^2 - v^2}} - \frac{\dot{v}V}{V\sqrt{V^2 - v^2}} \\ &= \frac{\dot{v}}{\sqrt{u^2 + w^2}} - \frac{v\left(u\dot{u} + v\dot{v} + w\dot{w}\right)}{\left(u^2 + v^2 + w^2\right)\sqrt{u^2 + w^2}} \end{aligned} \tag{28}$$

From the flight dynamics, the following equations hold:

$$\begin{bmatrix} \dot{u} \\ \dot{v} \\ \dot{w} \end{bmatrix} = \frac{1}{m}\begin{bmatrix} X \\ Y \\ Z \end{bmatrix} - \begin{bmatrix} qw - rv \\ ru - pw \\ pv - qu \end{bmatrix} + g\begin{bmatrix} \sin\theta \\ \sin\phi\sin\theta \\ \cos\phi\cos\theta \end{bmatrix} \tag{29}$$

Substituting Eq. 29 into the first term of Eq. 28 results in:

$$\begin{aligned} \frac{\dot{v}}{\sqrt{u^2 + w^2}} &= \frac{1}{\sqrt{u^2 + w^2}}\left(\frac{Y}{m} - ru + pw + g\sin\phi\cos\theta\right) \\ &= \frac{1}{\sqrt{u^2 + w^2}}\left(\frac{Y}{m} + g\sin\phi\cos\theta\right) + \begin{bmatrix} \frac{w}{\sqrt{u^2 + w^2}} & 0 & \frac{-u}{\sqrt{u^2 + w^2}} \end{bmatrix}\begin{bmatrix} p \\ q \\ r \end{bmatrix} \end{aligned} \tag{30}$$

By substitution, the second term of Eq. 28 becomes:

$$\begin{aligned} \frac{v\left(u\dot{u} + v\dot{v} + w\dot{w}\right)}{V^2\sqrt{u^2 + w^2}} &= \frac{v}{V^2\sqrt{u^2 + w^2}}\left\{u\left[\frac{X}{m} - (qw - rv) - g\sin\theta\right]\right. \\ &\left. + v\left[\frac{Y}{m} - (ru - pw) + g\sin\phi\cos\theta\right] + w\left[\frac{Z}{m} - (pv - qu) + g\cos\phi\cos\theta\right]\right\} \end{aligned} \tag{31}$$

Eq. 31 can be further simplified as:

$$\begin{aligned} \frac{v\left(u\dot{u} + v\dot{v} + w\dot{w}\right)}{V^2\sqrt{u^2 + w^2}} &= \frac{v}{V^2\sqrt{u^2 + w^2}}\left[u\left(\frac{X}{m} - g\sin\theta\right) + v\left(\frac{Y}{m} + g\sin\phi\cos\theta\right) + w\left(\frac{Z}{m} + g\cos\phi\cos\theta\right)\right. \\ &\qquad \left. - (qw - rv) - (ru - pw) - (pv - qu)\right] \\ &= \frac{v}{V^2\sqrt{u^2 + w^2}}\left[u\left(\frac{X}{m} - g\sin\theta\right) + v\left(\frac{Y}{m} + g\sin\phi\cos\theta\right) + w\left(\frac{Z}{m} + g\cos\phi\cos\theta\right)\right] \end{aligned} \tag{32}$$

Combining Eq. 30 with Eq. 32 yields:

$$\begin{aligned}
\dot{\beta} =& \frac{1}{\sqrt{u^2+w^2}}\left(\frac{Y}{m}+g\sin\phi\cos\theta\right)+\begin{bmatrix}\frac{w}{\sqrt{u^2+w^2}} & 0 & \frac{-u}{\sqrt{u^2+w^2}}\end{bmatrix}\begin{bmatrix}p\\q\\r\end{bmatrix}\\
&-\frac{v}{V^2\sqrt{u^2+w^2}}\left[u\left(\frac{X}{m}-g\sin\theta\right)+v\left(\frac{Y}{m}+g\sin\phi\cos\theta\right)+w\left(\frac{Z}{m}+g\cos\phi\cos\theta\right)\right]\\
=& \frac{1}{\sqrt{u^2+w^2}}\left[\frac{-uv}{V^2}\left(\frac{X}{m}-g\sin\theta\right)+\left(1-\frac{v}{V^2}\right)\left(\frac{Y}{m}+g\sin\phi\cos\theta\right)-\frac{vw}{V^2}\left(\frac{Z}{m}+g\cos\phi\cos\theta\right)\right]\\
&+\begin{bmatrix}\frac{w}{\sqrt{u^2+w^2}} & 0 & \frac{-u}{\sqrt{u^2+w^2}}\end{bmatrix}\begin{bmatrix}p\\q\\r\end{bmatrix}\\
=& \frac{1}{\sqrt{u^2+w^2}}\left[\frac{-uv}{V^2}\left(A_x-g\sin\theta\right)+\left(1-\frac{v}{V^2}\right)\left(A_y+g\sin\phi\cos\theta\right)-\frac{vw}{V^2}\left(A_z+g\cos\phi\cos\theta\right)\right]\\
&+\begin{bmatrix}\frac{w}{\sqrt{u^2+w^2}} & 0 & \frac{-u}{\sqrt{u^2+w^2}}\end{bmatrix}\begin{bmatrix}p\\q\\r\end{bmatrix}
\end{aligned} \tag{33}$$

with A_x, A_y and A_z defined in Sec. III A.

References

[1] Smaili, M., Breeman, J., Lombaerts, T., and Joosten, D., "A Simulation Benchmark for Integrated Fault Tolerant flight Control Evaluation," *AIAA paper 2006-6471*, Aug. 2006.

[2] "Civil Aviation Safety Data," Technical report, Civil Aviation Authority of the Netherlands, Netherlands, 2003.

[3] Lombaerts, T. J., Van Oort, E. R., and Chu, Q. P., "Online Aerodynamic Model Structure Selection and Parameter Estimation for Fault-Tolerant Control," *Journal of Guidance, Control and Dynamics*, Vol. 23, No. 5, 2010, pp. 812–818.

[4] Alwi, H., Edwards, C., Stroosma, O., and Mulder, J. A., "Evaluation of a Sliding Mode Fault-Tolerant Flight Controller for the El Al Incident," *Journal of Guidance, Control and Dynamics*, Vol. 33, No. 3, 2010, pp. 677–694.

[5] Lombaerts, T. J., Smaili, M. H., and Stroosma, O., "Piloted Simulator Evaluation results of New Fault-Tolerant Flight Control Algorithm," *Journal of Guidance, Control and Dynamics*, Vol. 32, No. 6, 2009,

pp. 1747–1765.

[6] Patton, R., "Fault Tolerant Control Systems: The 1997 Situation," *Proceedings of IFAC Symposium on SAFEPROCESS*, International Federation of Automatic Control, Laxenburg, Austria, 1997.

[7] Zhang, Y., "Fault Tolerant Control Systems:Historical Review and Current Research," technical paper, Centre de Recherche en Automatique de Nancy, Nancy, France, 2005.

[8] Zhang, Y. and Jiang, J., "Bibliographical Review on Reconfigurable Fault-Tolerant Control Systems," *5th IFAC Symposium on Fault Detection, Supervision and Safety for Technical Processes*, International Federation of Automatic Control, Laxenburg, Austria, 2003.

[9] Sonneveldt, L., Van Oort, E. R., Chu, Q. P., and Mulder, J. A., "Nonlinear Adaptive Trajectory Control Applied to an F-16 Model," *Journal of Guidance, Control and Dynamics*, Vol. 32, No. 1, 2009, pp. 25–39.

[10] van Oort, E. R., Sonneveldt, L., Chu, Q. P., and Mulder, J. A., "Full-Envelope Modular Adaptive control of a Fighter Aircraft Using Orthogonal Least Squares," *Journal of Guidance, Control and Dynamics*, Vol. 33, No. 5, 2010, pp. 1461–1472.

[11] Fuller, J. W., "Integrated Flight Propulsion Control for Loss-of-Control Prevention," *AIAA Guidance, Navigation and Control Conference*, AIAA, Minneapolis, Minnesota, 2012.

[12] Gilyard, G. B., Conley, J. L., Le, J., and Burcham, J. F. W., "A Simulation Evaluation of a Four–Engine Jet Transport Using Engine Thrust Modulation for Flightpath Control," *AIAA Guidance, Navigation and Control Conference*, AIAA, Toronto, Ontario Canada, 1991.

[13] Burcham, S., Kalmanje, K., and Nhan, N., "Adaptive Control of a Transport Aircraft using Differential Thrust," Nasa/tm-1998-206552, NASA Ames Research Center, May 1998.

[14] Vahram, S., Kalmanje, K., and Nhan, N., "Adaptive Control of a Transport Aircraft using Differential Thrust," Nasa technical paper 1108, NASA Ames Research Center, Moffett Field, Aug. 2009.

[15] Hovakimyan, N., Lavretsky, E., and Sasane, A., "Dynamic Inversion for Nonaffine-in-control systems via time-scale separation," *Journal of Guidance, Control and Dynamics*, Vol. 13, No. 4, 2007, pp. 451–465.

[16] Falkena, W., van Oort, E., and Chu, Q., "Towards Certifiable Advanced Flight Control Systems, A Sensor Based Backstepping Approach," *AIAA Guidance, Navigation and Control Conference*, AIAA, Portland, Oregon, 2011.

[17] Smaili, M., Breeman, J., Lombaerts, T., and Joosten, D., "A simulation benchmark for integrated fault tolerant flight control evaluation," Aiaa paper 2006-6471, AIAA, Aug. 2006.

[18] Smaili, M., Breeman, J., and Lombaerts, T., "A simulation benchmark for Aircraft Survivability Assessment," *26th International Congress of Aeronautical Sciences*, The International Council of the

Aeronautical Science, Anchorage, Alaska, 2008, pp. 1–12.

[19] Lombaerts, T. J., *Fault Tolerant Flight Control-A Physical Model Approach*, Ph.D. thesis, Delft University of Technology, The Netherlands, May 2010, pp.248-252.

[20] Mulder, J. A., *Designed and evaluation of dynamic flight test manoeuvers*, Ph.D. thesis, Delft University of Technology, The Netherlands, Oct. 1986.

[21] Halim, A., *Fault Tolerant Sliding mode Control Schemes with Aerospace Applications*, Ph.D. thesis, University of Leicester, England, Feb. 2008.

[22] Slotine, J.-J. E. and Li, W., *Applied Nonlinear Control*, Prentice Hall, New Jersey, 1991.

[23] Falkena, W., *Investigation of Practical Flight Control Systems for Small Aircraft*, Ph.D. thesis, Delft University of Technology, The Netherlands, Dec. 2012, pp.131-158.

[24] Khalil, H. K., *Nonlinear Systems*, Prentice Hall, New Jersey, 2002.

[25] Voth, C. and Ly, U.-L., "Total energy control system autopilot design with constrained parameter optimization," *American Control Conference*, IEEE, San Diego, California, 1990, pp. 1332–1337.

[26] Lombaerts, T. and Looye, G. H. N., "Design and flight testing of nonlinear autoflight control laws," *AIAA Guidance, Navigation and Control Conference*, AIAA, Minneapolis, Minnesota, 2012.

[27] Farrell, J., Sharma, M., and Polycarpou, M., "Backstepping-Based flight control with adaptive function approximation," *Journal of Guidance, Control and Dynamics*, Vol. 28, No. 6, 2005, pp. 1089–1102.